arXiv:1601.05782v1 [physics.plasm-ph] 21 Jan 2016

First-Principles Equation of State and Electronic Properties of Warm Dense Oxygen

K. P. Driver,[1] F. Soubiran,[1] Shuai Zhang,[1] and B. Militzer[1,2]

[1)] *Department of Earth and Planetary Science, University of California, Berkeley, California 94720, USA*[a)]

[2)] *Department of Astronomy, University of California, Berkeley, California 94720, USA*

(Dated: 22 January 2016)

We perform all-electron path integral Monte Carlo (PIMC) and density functional theory molecular dynamics (DFT-MD) calculations to explore warm dense matter states of oxygen. Our simulations cover a wide density-temperature range of $1-100$ g cm^{-3} and 10^4-10^9 K. By combining results from PIMC and DFT-MD, we are able to compute pressures and internal energies from first-principles at all temperatures and provide a coherent equation of state. We compare our first-principles calculations with analytic equations of state, which tend to agree for temperatures above 8×10^6 K. Pair-correlation functions and the electronic density of states reveal an evolving plasma structure and ionization process that is driven by temperature and density. As we increase the density at constant temperature, we find that the ionization fraction of the 1s state decreases while the other electronic states move towards the continuum. Finally, the computed shock Hugoniot curves show an increase in compression as the first and second shells are ionized.

[a)]Electronic mail: kdriver@berkeley.edu; http://militzer.berkeley.edu/~driver/

I. INTRODUCTION

Elemental oxygen is involved in a wide range of physics and chemistry throughout the universe, spanning from ambient biological processes to extreme geological and astrophysical processes. Created during stellar nucleosynthesis, oxygen is the third most abundant element in the universe and the most abundant element on Earth. In addition to its importance for life-sustaining processes, its thermodynamic, physical, and chemical properties are important to numerous fields of science. As such, oxygen has inspired a vast number of laboratory experiments and theoretical studies, which have revealed an exotic phase diagram with a number of interesting anomalies in its thermal, optical, magnetic, electrical, and acoustic properties due to its molecular and magnetic nature[1].

At ambient conditions, oxygen exists as a diatomic molecular gas with each molecule having two unpaired electrons, resulting in a paramagnetic state. X-ray diffraction and optical experiments reveal that oxygen condenses to a molecular solid with a rich phase diagram made up of at least ten different structural phases[1–6]. Static compression experiments on the solid have been performed up to 1.3 Mbar and 650 K[1]. First-principles simulations have been used to search for structural phases up to 100 Mbar[6]. The transition to the highest-pressure phase discovered so far occurs at 96 GPa, which also drives the solid to become metallic[7–10]. A superconducting phase has also been found at 0.6 K near 100 GPa[11]. In addition, the solid phases exhibit a complex magnetic structure with various degrees of ordering due to a strong exchange interaction between O_2 molecules that becomes suppressed under pressure and acts in tandem with weak van der Waals forces holding the lattice together[1,12,13].

Warm, dense, fluid states of oxygen have also been of great interest due to the presence of oxygen-rich compounds in inner layers of giant planets[19–23], stellar interiors[24,25], astrophysical processes[26–28], and detonation products[29]. Oxygen is produced via helium burning[30] in the late stages of Sun-like star's life as well as in more massive stars. The larger weight of oxygen relative to hydrogen and helium drives its settlement towards the deepest regions of a star. An accurate equation of state (EOS) is needed to properly describe the behavior of the core of the star as well as the timing of the different nuclear processes that are highly sensitive to temperature[30,31]. Eventually, intermediate mass stars evolve into white dwarfs, which have most of their hydrogen and helium depleted, leaving a remnant composed mostly of carbon and oxygen. The core density of a white dwarf[16] is likely higher than 10^5 g/cm^3.

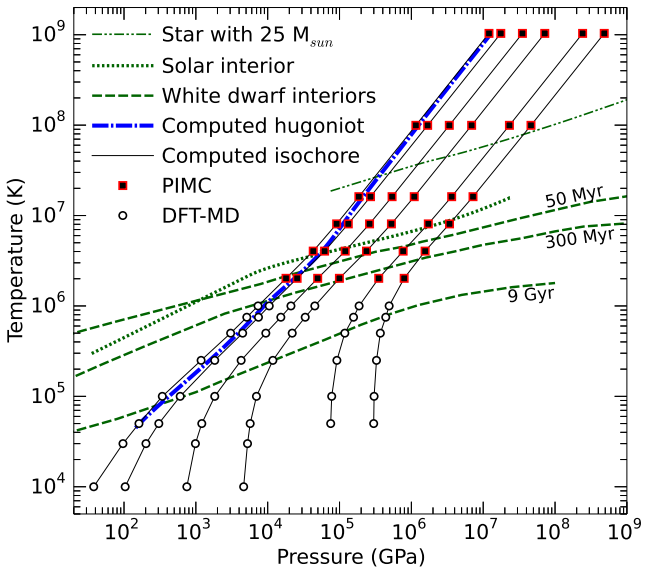

FIG. 1. Temperature-pressure conditions for the PIMC and DFT-MD calculations along six isochores corresponding to the densities of 2.48634, 3.63046, 7.26176, and 14.8632, 50.00, and 100.00 g cm^{-3}. The dash-dotted line shows the Hugoniot curve for an initial density of $\rho_0 = 0.6671$ g cm^{-3}. For comparison, we also plotted the interior profile of the current-day Sun[14] as well as the profile of a 25 M$_\odot$ star at the end of its helium burning time[15]. The green dashed lines show the interior profile of a 0.6 M$_\odot$ carbon-rich white dwarf at three different stages of its cooling process[16–18]

The cooling process of the white dwarf is very similar from one white dwarf to another and the luminosity is used for cosmological chronology[32,33]. However, the accuracy of chronology measurements depends on a proper description of the thermodynamic behavior of both carbon and oxygen[34]. Moreover, as the third most abundant element in the solar system[35], oxygen has a significant presence in planet interiors and can exist in a partially ionized state in giant planets. Therefore, the electronic and thermodynamic behavior of oxygen at high pressures and temperatures is important for obtaining the correct fluid and magnetic behavior in planetary, stellar, and stellar remnant models[36].

Shock-compressed fluid states of oxygen have been measured under dynamic compression up to 1.9 Mbar (four-fold compression) and 7000 K, which revealed a metallic transition in the molecular fluid at 1.2 Mbar and 4500 K[37]. Density functional theory molecular dynamics (DFT-MD) simulations suggest that disorder in the fluid lowers the metallization pressure to as low as 30 GPa with molecular dissociation above 80 GPa[38]. Measurements of

Hugoniots have reached 140 GPa[39–41] and indicate that oxygen molecules become dissociated in a pressure range of 80-120 GPa at temperatures over several thousand Kelvin. Using classical pair-potential simulations[42–44], some general agreement is found with the measured Hugoniots, however, a fully quantum-mechanical treatment is needed to accurately simulate the electronic and structural behavior of the fluid.

Historically, a lack of development in first-principles methodology for the warm dense matter regime has largely prevented highly accurate theoretical exploration of fluid oxygen at extreme conditions, and, hence, further improvements in EOS and Hugoniot curves. DFT-MD has been used to explore the structural and electronic behavior of the fluid state[38,45] up to temperatures of 16×10^3 K and densities up to 4.5 g cm^{-3}. Massacrier *et al.*[46] investigated the properties of oxygen for a density-temperature range of $10^{-3}-10^4$ g cm^{-3} and 10^5-10^6 K, using an average ion model. They showed, for instance, that the complete pressure-ionization of fluid oxygen cannot be expected until the system reaches a density of 1000 g cm^{-3}.

In order to address the challenges of first-principles simulations for warm dense matter, we have been developing the path integral Monte Carlo (PIMC) methodology in recent years for the study of heavy elements in warm, dense states[47–50]. Here, we apply our PIMC methodology along with DFT-MD to extend the first principles exploration of warm dense fluid oxygen to a much wider density-temperature range (1–100 g cm^{-3} and 10^4–10^9 K) than has been previously explored by DFT-MD alone.

In Section II, we cover details of the PIMC and DFT-MD methodology specific to our oxygen simulations. In Section III, we discuss the EOS constructed from PIMC and DFT-MD and show that both methods agree for at least one of temperature in the range of 2.5×10^5–1×10^6 K. In section IV, we characterize the structure of the plasma and the ionization process by examining pair-correlation functions of electrons and nuclei as a function of temperature and density. In section V, we discuss the electronic density of states as a function of density and temperature to provide further insight into the ionization process. In section VI, we discuss predictions for the shock Hugoniot curves. Finally, in section VII, we summarize and conclude our results.

II. SIMULATION METHODS

PIMC[47,51] is currently the state-of-the-art first-principles method for simulating materials at temperatures in which properties are dominated by excited states. It is the only method able to accurately treat all the effects of bonding, ionization, exchange-correlation, and quantum degeneracy that simultaneously occur in the warm dense matter regime[52]. PIMC is based on thermal density matrix formalism, which is efficiently computed with Feynman's imaginary time path integrals. The density matrix is the natural operator to use for computing high-temperature observables because it explicitly includes temperature in a many-body formalism.

The PIMC method stochastically solves the full, finite-temperature quantum many-body problem by treating electrons and nuclei equally as quantum paths that evolve in imaginary time without invoking the Born-Oppenheimer approximation. For our PIMC simulations, the Coulomb interaction is incorporated via pair density matrices derived from the eigenstates of the two-body Coulomb problem[51,53] appropriate for oxygen. Furthermore, in contrast to DFT-MD as described below, the efficiency of PIMC increases with temperature as particles behave more classical-like and fewer time slices are needed to describe quantum mechanical many-body correlations, scaling inversely with temperature.

PIMC uses a minimal number of controlled approximations, which become vanishingly small with increased temperature and by using appropriate convergence of the time-step and system size. The only uncontrolled approximation is the employment of a fixed nodal surface to avoid the fermion sign problem[54]. Current state-of-the art PIMC calculations employ a free-particle nodal structure, which would perfectly describe a fully ionized system. However, we have shown PIMC employing free-particle nodes even produces reliable results at surprising low temperatures in partially ionized hydrogen[55], carbon[48], water[48], and neon[50]. As a general rule, we find free-particle nodes are sufficient for systems comprised of partially-ionized 2s states[48].

A sufficiently small PIMC time step is determined by converging total energy as a function of time step until the energy changes by less than 0.5%, which is shown in supplemental material[56] Table SI. We use a time step of 1/256 Ha^{-1} for temperatures below $4{\times}10^6$ K and, for higher temperatures, we decrease the time step as $1/T$, as the efficiency of PIMC increases linearly with T as path lengths decrease. The number of time slices we use in

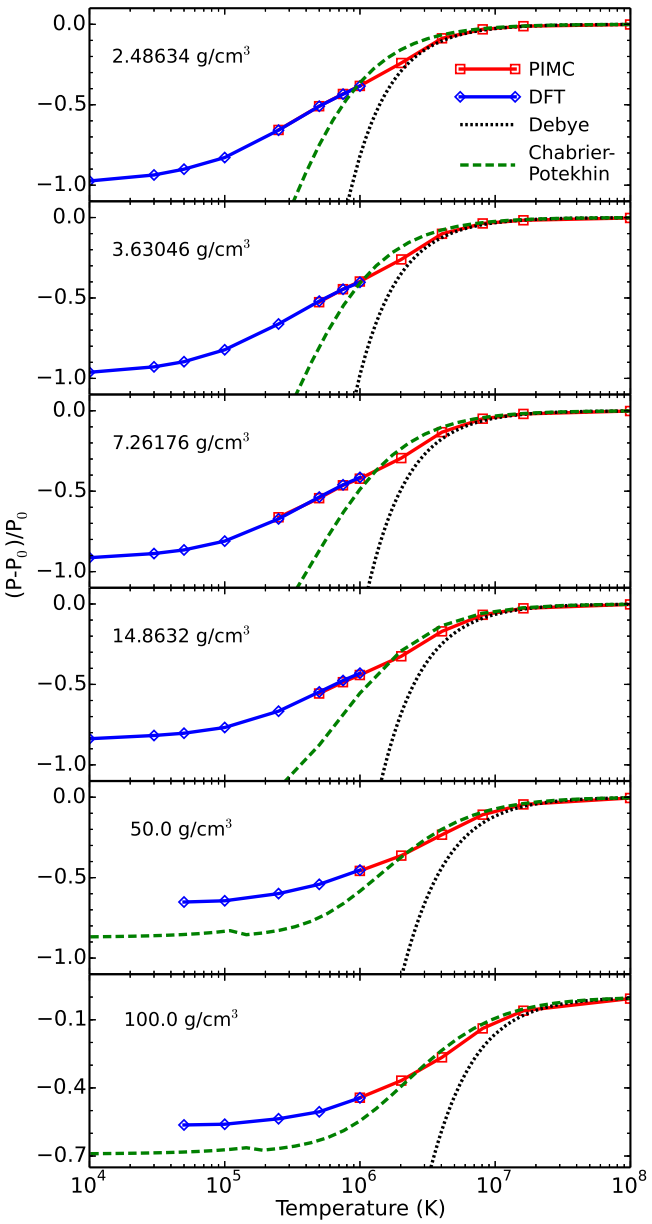

FIG. 2. Comparison of excess pressure relative to the ideal Fermi gas plotted as a function of temperature for oxygen.

the path integral range from 323 at lowest temperature to 5 at the highest temperature. In order to minimize finite size errors, the internal energy and pressure is converged to better than 0.4% when comparing 8- and 24-atom simple cubic simulation cells, which is shown in supplemental material[56] Table SII. We therefore perform all PIMC calculations in 8-atom cells, as PIMC scales as N^2, where N is the number of particles. A typical calculation uses a bisection level[51] of 5 and achieves a statistical error in the energy and pressure that is less

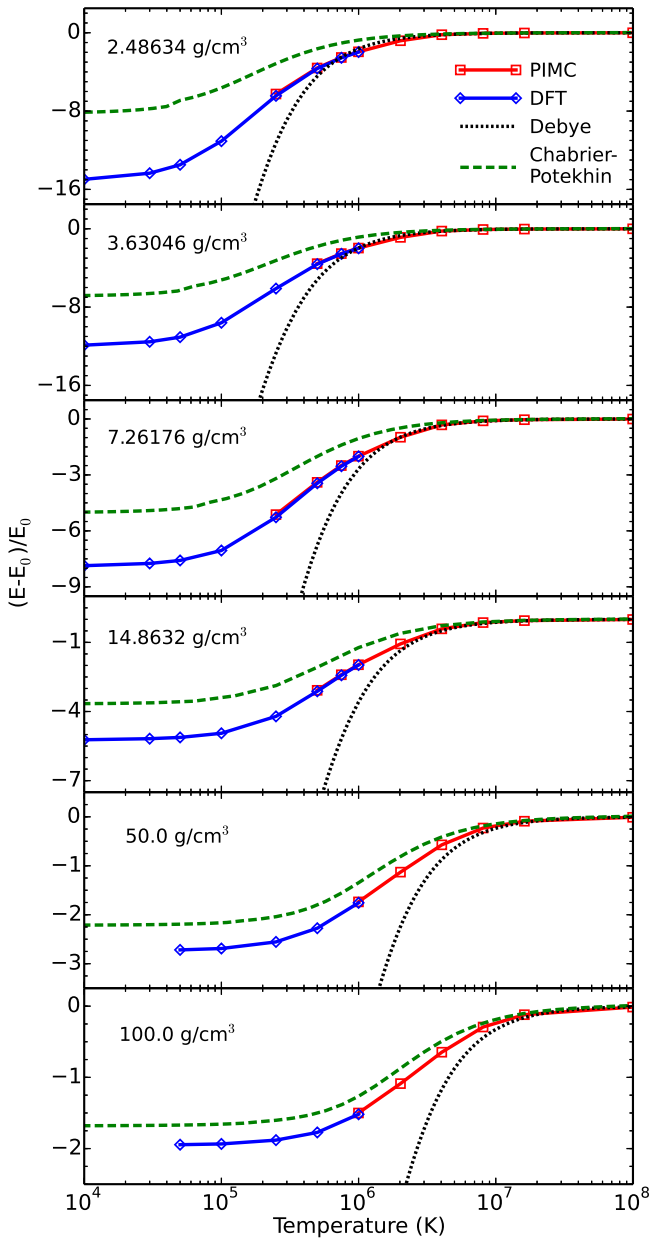

FIG. 3. Comparison of excess internal energies relative to the ideal Fermi gas plotted as a function of temperature for oxygen.

than 0.1%.

For lower temperatures (T $<$ 1×10^6 K), DFT-MD[57] is the most efficient state-of-the-art first-principles method. DFT formalism provides an exact mapping of the many body problem onto a single particle problem, but, in practice, employs an approximate exchange-correlation potential to describe many body electron physics. In the WDM regime, where

temperatures are at or above the Fermi temperature, the exchange-correlation functional is not explicitly designed to accurately describe the electronic physics[58]. However, in previous PIMC and DFT-MD work on helium[47] carbon[48], and water[48], and neon[50], DFT functionals are shown to be accurate even at high temperatures.

DFT incorporates effects of finite electronic temperature into calculations by using a Fermi-Dirac function to allow for thermal occupation of single-particle electronic states[59]. As temperature grows large, an increasing number of bands are required to account for the increasing occupation of excited states in the continuum, which typically causes the efficiency of the algorithm to become intractable at temperatures beyond 1×10^6 K. Orbital-free density functional methods aim to overcome such thermal band efficiency limitations, but several challenges remain to be solved[60]. In addition, pseudopotentials, which replace the core electrons in each atom and improve efficiency, may break down at temperatures where core electrons undergo excitations.

Depending on the density, we employ two different sets of DFT-MD simulations for our study of oxygen. At densities below 15 g cm^{-3}, the simulations were performed with the Vienna *Ab initio* Simulation Package (VASP)[61] using the projector augmented-wave (PAW) method[62]. The VASP DFT-MD uses a NVT ensemble regulated with a Nosé-Hoover thermostat. Exchange-correlation effects are described using the Perdew-Burke-Ernzerhof[63] generalized gradient approximation. Electronic wave functions are expanded in a plane-wave basis with a energy cut-off of at least 1000 eV in order to converge total energy. Size convergence tests up to a 24-atom simulation cell at temperatures of 10,000 K and above indicate that total energies are converged to better than 0.1% in a 24-atom simple cubic cell. We find, at temperatures above 250,000 K, 8-atom supercell results are sufficient since the kinetic energy far outweighs the interaction energy at such high temperatures. The number of bands in each calculation is selected such that thermal occupation is converged to better than 10^{-4}, which requires up to 8,000 bands in a 24-atom cell at 1×10^6 K. All simulations are performed at the Γ-point of the Brillouin zone, which is sufficient for high temperature fluids, converging total energy to better than 0.01% relative to a comparison with a grid of k-points.

For densities above 15 g cm^{-3}, we had to construct a new pseudopotential in order to prevent the overlap of the PAW-spheres. We therefore used the ABINIT package[64] for which it is possible to build a specific PAW-pseudopotential using the AtomPAW plugin[65]. We built

a hard all-electron PAW pseudopotential with a cut-off radius of 0.4 Bohr. We checked the accuracy of the pseudopotential by reproducing the results provided by the ELK software in the linearized augmented plane wave (LAPW) framework[66]. With this pseudopotential we performed DFT-MD with ABINIT for a 24-atom cell up to 100 g cm^{-3} and 1×10^6 K. The hardness of the pseudopotential required an plane-wave energy cut-off of at least 6800 eV.

III. EQUATION OF STATE RESULTS

In this section, we report our EOS results for six densities of 2.48634, 3.63046, 7.26176, and 14.8632, 50.00, and 100.00 g cm^{-3} and for a temperature range of $10^4 - 10^9$ K. The six isochores are shown in Figure 1 and are discussed in more detail in section VI. These conditions are relevant for the modeling of stars and white dwarfs as can be seen in Figure 1.

Figure 2 compares pressures obtained for oxygen from PIMC, DFT-MD, and from analytic Chabrier-Potekhin[67] and Debye-Hückel[68] models. Pressures, P, are plotted relative to a fully ionized Fermi gas of electrons and ions with pressure, P_0, in order to compare only the excess pressure contributions that result from particle interactions. In general PIMC and DFT-MD pressures differ by at most 2%, and often much less for at least one temperature in the range of $2.5 \times 10^5 - 1 \times 10^6$ K. PIMC converges to the weakly interacting plasma limit along with the Chabrier-Potekhin and Debye-Hückel models.

Figure 3 compares internal energies, E, plotted relative to the internal energy of a fully ionized Fermi gas, E_0. PIMC and DFT-MD results for excess internal energy differ by at most 2%, and much less in most cases for at least one temperature in the range of $2.5 \times 10^5 - 1 \times 10^6$ K. PIMC extends the energies to the weakly interacting plasma limit at high temperatures, in agreement with the Potekhin and Debye-Hückel models[68].

Together, Figs. 2 and 3 show that the DFT-MD and PIMC methods form a coherent equation of state over all temperatures ranging from the regime of warm dense matter to the weakly interacting plasma limit. The agreement between PIMC and DFT-MD indicates that DFT exchange-correlation potential remains valid even at high temperatures and that the PIMC free-particle nodal approximation is valid for a sufficient ionization fraction of the 2s state. The analytic Chabrier-Potekhin and Debye-Hückel models agree with PIMC to temperatures as low as 8×10^6 K. The Debye-Hückel model appears to have better agreement with PIMC at low densities, while the Chabrier-Potekhin model agrees better with PIMC at

high densities. Neither analytic model includes bound states and, therefore, cannot describe low temperature conditions.

Table VII provides the densities, temperatures, pressures, and energies used to construct our equation of state. The VASP DFT-MD energies have been shifted by 74.9392 Ha/atom in order to bring the PAW-PBE pseudpotential energy in alignment with all-electron energies that we report with PIMC computations. The shift was calculated by performing an all electron atomic calculation with the OPIUM code[69] and a corresponding isolated-atom calculation in VASP.

Comparison of the PIMC and DFT-MD pressures and internal energies in Table VII indicates that there is roughly a 2% discrepancy in their predicted values at temperatures of 1×10^6 K. Potential sources of this discrepancy include: (1) the use of free particle nodes in PIMC; (2) the exchange-correlation functional in DFT; and (3) the use of a pseudopotential in DFT. While it is difficult to determine the size of the nodal and exchange-correlation errors, comparison of our VASP calculations with all-electron, PAW ABINIT calculations at 1×10^6 K indicates that roughly one third of the discrepancy is due to the use of frozen 1s core in the VASP DFT-MD pseudopotential, which leaves out effects of core excitations.

IV. PAIR-CORRELATION FUNCTIONS

In this section, we study pair-correlation functions[70] in order to understand the evolution of the fluid structure and ionization in oxygen plasmas as a function of temperature and density.

Figure 4 shows the nuclear pair-correlation functions, $g(r)$, computed with PIMC over a temperature range of $2 \times 10^6 - 1.034 \times 10^{12}$ K and a density range of $2.486 - 100.0$ $\mathrm{g\,cm^{-3}}$. Atoms are kept farthest apart at low temperatures due to a combination of Pauli exclusion among bound electrons and Coulomb repulsion. As temperature increases, kinetic energy of the nuclei increases, making it more likely to find atoms at close range, and, in addition, the atoms become increasingly ionized, which gradually minimizes the effects of Pauli repulsion. As density increases, the likelihood of finding two nuclei at close range is significantly increased. For the highest density and lowest temperature, the peak in the pair-correlation function reaches a value of 1.2, indicating a moderately structured fluid.

Figure 5 compares the nuclear pair-correlation functions of PIMC and DFT at a temper-

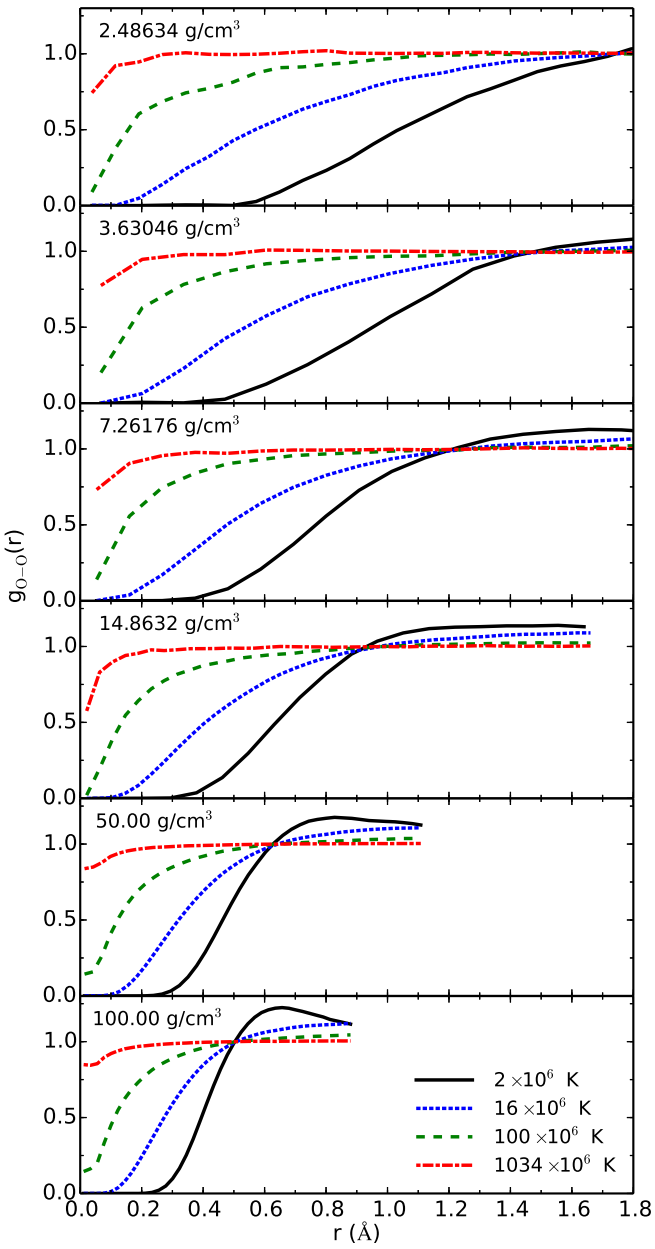

FIG. 4. Nuclear pair-correlation functions for oxygen from PIMC over a wide range of temperatures and densities.

ature of 1×10^6 K in an 8-atom cell at a density of 14.8632 g cm^{-3}. The overlapping $g(r)$ curves verify that PIMC and DFT predict consistent structural properties.

Figure 6 shows nucleus-electron pair correlation functions. Electrons are most highly correlated with the nuclei at low temperature and high density, reflecting a lower ionization fraction. As temperature increases, electrons are thermally excited and gradually become

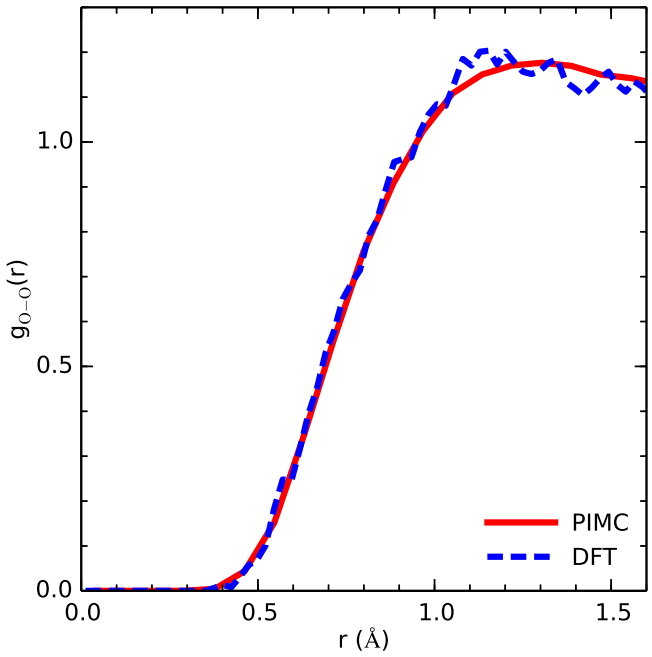

FIG. 5. Comparison of PIMC and DFT nuclear pair-correlation functions for oxygen at a temperature of $1{\times}10^6$ K and a density of 14.8632 g cm^{-3}.

unbound, decreasing their correlation with the nuclei. As the density is increased, the electrons are more likely to reside near the nuclei, indicating that the ionization of the 1s state is suppressed with increasing density.

Figure 7 shows the integral of the nucleus-electron pair correlation function, $N(r)$, which represents the average number of electrons within a sphere of radius r around a given nucleus,

$$N(r) = \left\langle \frac{1}{N_I} \sum_{e,I} \theta(r - |\vec{r}_e - \vec{r}_I|) \right\rangle, \tag{1}$$

where the sum includes all electron-ion pairs and *theta* represents the Heaviside function. At the lowest temperature, $1{\times}10^6$ K, we find that the 1s core state is always fully occupied, as it agrees closely with the result of an isolated 1s state. As temperature increases, the atoms are gradually ionized and electrons become unbound, causing $N(r)$ to decrease. As density increases, an increasingly higher temperature is required to fully ionize the atoms, confirming that the 1s ionization fraction decreases with density as seen in Fig. 6. The 1s state is thus not affected by pressure ionization in the density range of consideration. As we will explain the density of states section, the ionization of the 1s state is suppressed because with increasing density, the Fermi energy increases more rapidly than energy of the 1s state.

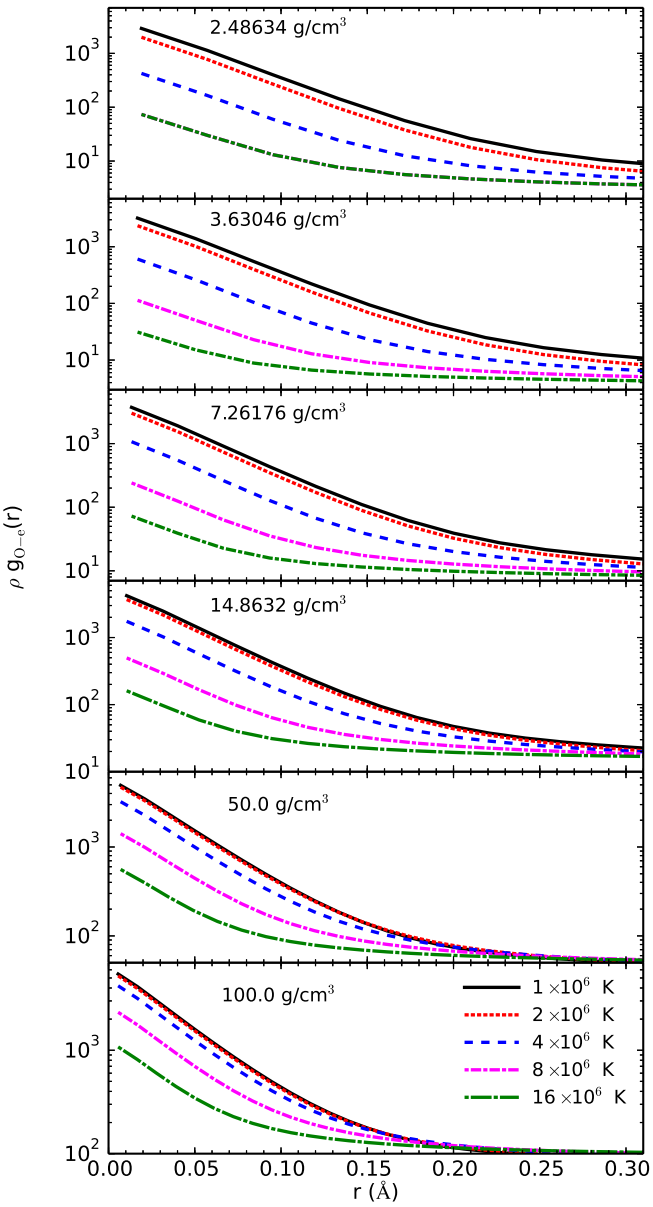

FIG. 6. The nucleus-electron pair-correlation functions for oxygen computed with PIMC.

Figure 8 shows electron-electron pair correlations for electrons having opposite spins. The function is multiplied by the particle density, ρ, in units of g cm^3, so that the integral under the curves is proportional to the number of electrons. The electrons are most highly correlated for low temperatures, which reflects that multiple electrons occupy bound states at one nucleus. As temperature increases, electrons are thermally excited, decreasing the correlation among each other. Correlation at short distances increases with density, consistent with a lower ionization fraction.

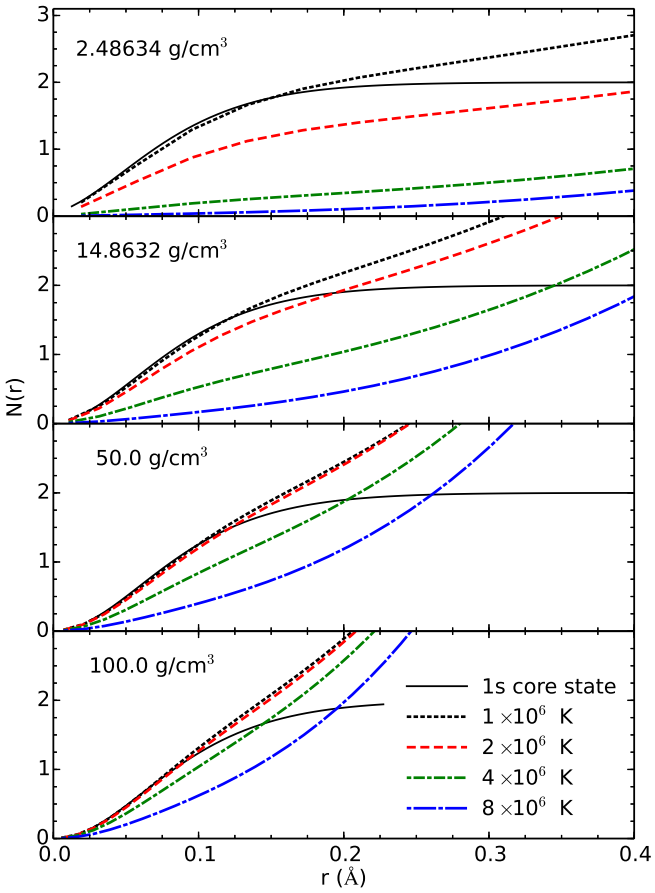

FIG. 7. Number of electrons contained in a sphere of radius, r, around an oxygen nucleus. PIMC data at four temperatures is compared with the analytic 1s core state.

Figure 9 shows electron-electron pair correlations for electrons with parallel spins. The positive correlation at at ∼2.5 Å for $T \leq 2 \times 10^6\,\mathrm{K}$ reflects that different electrons with parallel spins are bound to a single nucleus. For short separations, Pauli exclusion takes over and the functions decay to zero. The ordering of the g(r) curves changes with respect to temperature as density increases due to a competition between Coulomb and kinetic effects, coupled with the effects of ionization. When the density is 50 and 100 $\mathrm{g\,cm^{-3}}$, pressure ionization causes the correlation to approach that of an ideal fluid, and increasing temperature further only strengthens kinetic effects. We interpret this change as pressure ionization of the second and third electron shells. As temperature increases, electrons become less bound, which also causes the correlation to become more like an ideal fluid.

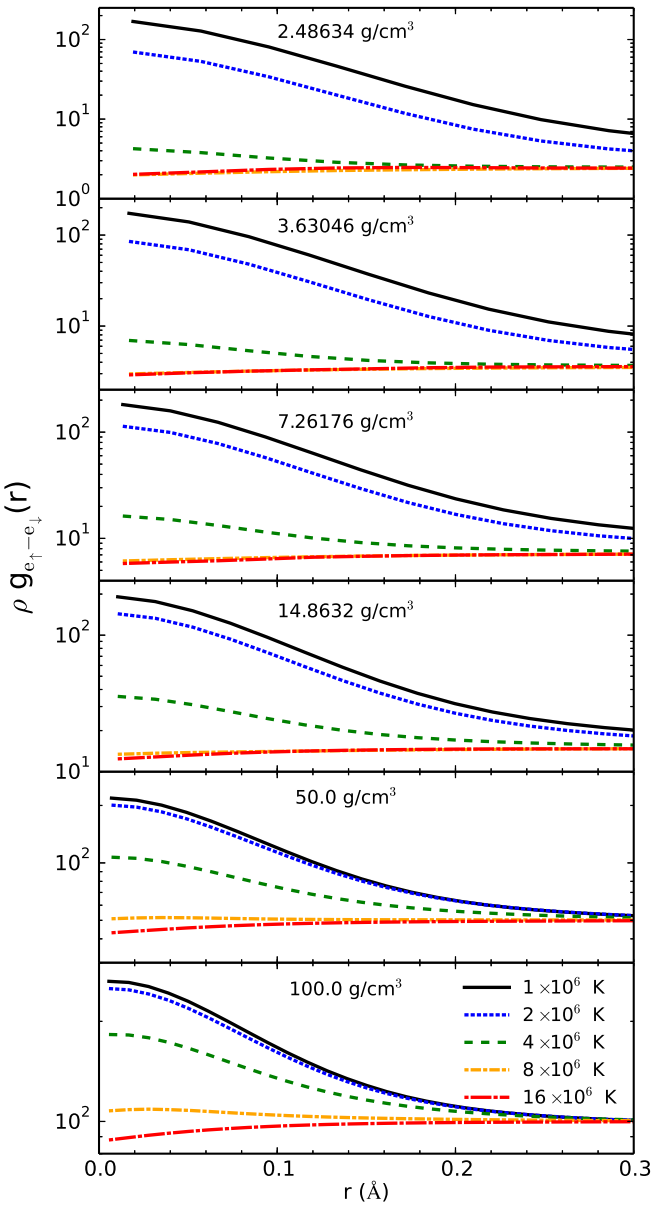

FIG. 8. The electron-electron pair-correlation functions (multiplied by ρ) for electrons with opposite spins computed with PIMC.

V. ELECTRONIC DENSITY OF STATES

In this section, we report DFT-MD results for the electronic density of states (DOS) of fluid oxygen as a function of temperature and density in order to gain further insight into the temperature- and pressure-ionization.

In order to closely examine the physics of pressure-ionization of the 1s and higher states,

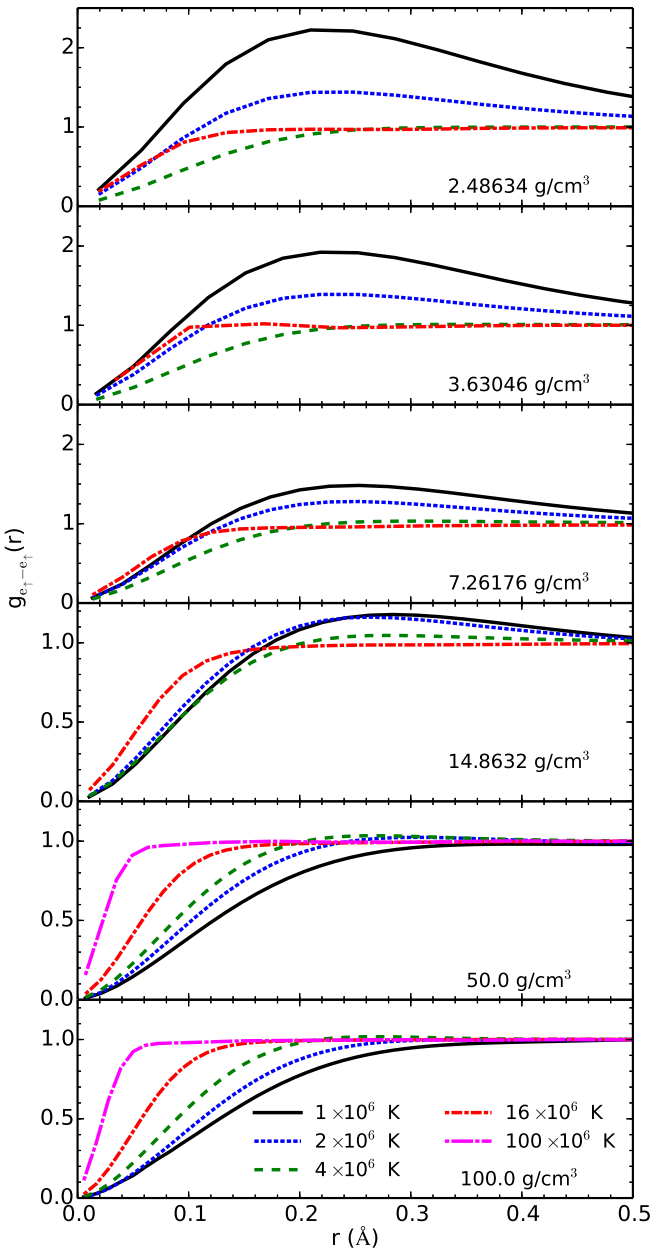

FIG. 9. The electron-electron pair-correlation functions for electrons with parallel spins computed with PIMC.

we computed DOS curves using the all-electron, PAW potential we created for use with the ABINIT code. Figure 10 shows examples of the DOS for oxygen at densities between 2.49 and 100 $\mathrm{g\,cm^{-3}}$ at a fixed temperature of 100,000 K. For comparison, we show the result for an isolated oxygen atom. Since we used the all-electron pseudo-potential we can see the bands related to the 1s or K shell. For the isolated atom, we also clearly see the 2s or $\mathrm{L_I}$ as

well as the L_{II} and L_{III} states. The locations of the K and L_I shells for the isolated atom are consistent with the binding energies of 19.97 and 1.53 Ha respectively that can be found in the literature[71].

As density increases, the L sub-shells are shifted towards higher energy, merging together as they shift into the continuum. This effect is referred to as the pressure ionization of oxygen, also described by Massacrier *et al.*[46]. As the density increases, the K shell is also shifted to higher energies and broadens significantly. Nevertheless, the K shell remains a well defined state even at 100 $\mathrm{g\,cm^{-3}}$. The Fermi energy is also shifted towards higher energy values as the density increases. We observe that the Fermi energy shifts more than the K-shell energy, and, hence, the energy difference between the 1s states and unoccupied states increases with the density. Therefore, it is more difficult to temperature-ionize the K shell at higher density and no pressure-ionization occurs for the 1s state. This is consistent with the observations we made for the electron-nuclei pair distribution function in Fig. 6.

Figure 11 shows the temperature dependence of the DOS at a fixed density of 7.26176 $\mathrm{g\,cm^{-3}}$. Results were obtained from VASP by averaging over at least 10 uncorrelated snapshots chosen from a DFT-MD trajectory. Smooth curves were obtained by using a 4×4×4 k-point grid and applying a Gaussian smearing of 2 eV. The eigenvalues of each snapshot were shifted so that the Fermi energies align at zero, and the integral of the DOS is normalized to 1. The DOS curves show a large peak representing the atomic-like 2s and 2p states, followed by a dip in states, which is then followed by a continuous spectrum of conducting states. The Fermi energy plays the role of the chemical potential in the Fermi-Dirac distribution, which shifts towards more negative values as the temperature is increased. Because we subtract the Fermi energy from the eigenvalues, the peak shifts to higher energies with increasing temperature. The fact that the peaks are embedded into a dense, continuous spectrum of eigenvalues indicates that they are conducting states.

VI. SHOCK COMPRESSION

Dynamic shock compression experiments are widely used for measuring equation of state and other physical properties of hot, dense fluids. Commonly, shock experiments determine the Hugoniot, which is the locus of final states that can be obtained from different shock velocities. A few Hugoniot measurements have been made for oxygen in an effort to under-

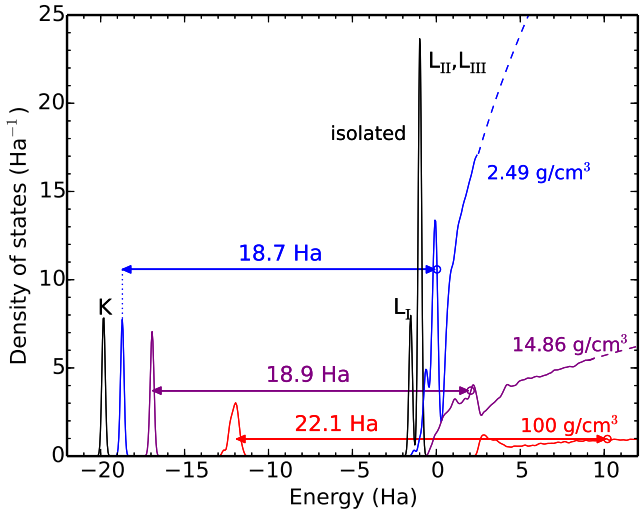

FIG. 10. Electronic density of states of dense, fluid oxygen using an all-electron, PAW pseudopotential. The solid lines represent all available states for the isolated atom as well as three other densities at a temperature of 1×10^5 K. The curves are normalized such that the occupied DOS integrates to 8. The K, L_I, L_{II} and L_{III} identify the electronic shells and sub-shells for the isolated atoms. The open circle on each curve stands for the DOS at the Fermi energy level. The arrows show the energy difference between the K-shell and the Fermi energy for the different densities.

stand its metallic transition and determine its role in astrophysical processes[39–41]. Density functional theory has been validated by experiments as an accurate tool for predicting the shock compression of different materials[45,72].

In the course of a shock wave experiment, a material whose initial state is characterized by an internal energy, pressure, and volume, (E_0, P_0, V_0), which changes to a final state denoted by (E, P, V) while conserving mass, momentum, and energy. This leads to the Rankine-Hugoniot relation[73],

$$H = (E - E_0) + \frac{1}{2}(P + P_0)(V - V_0) = 0. \tag{2}$$

Here, we compute the Hugoniot for oxygen from the first-principles EOS data we showed in Table VII. The pressure and internal energy data points were interpolated with bi-cubic spline functions in $\rho - T$ space. For the initial state of the principal Hugoniot curve, we computed the energy of an oxygen molecule at $P_0 = 0$, $E_0 = -150.247327$ Ha/O_2, and chose $V_0 = 318.612$ Å^3. We chose a density of 0.6671 g cm^{-3} for solid oxygen in the cubic, γ phase.

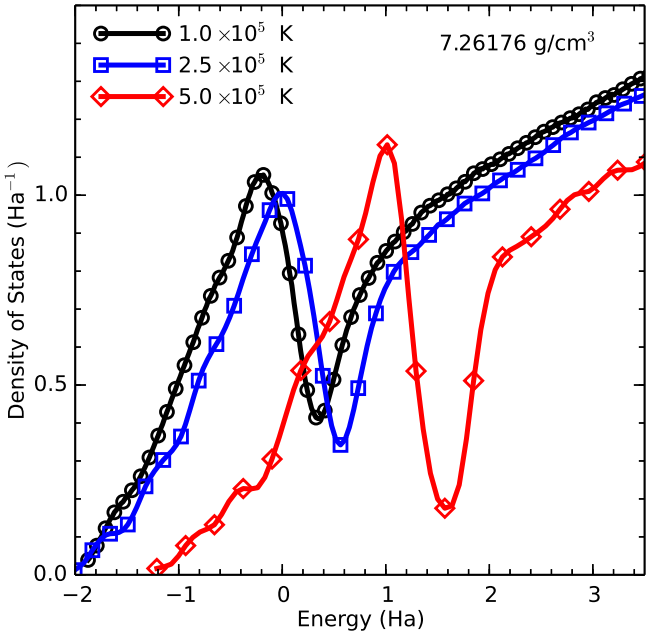

FIG. 11. Total electronic DOS of dense, fluid oxygen at a fixed density of 7.26176 g cm^{-3} for three temperatures (1×10^5, 2.5×10^5 and 5×10^5 K). Each DOS curve has had the relevant Fermi energy for each temperature subtracted from it.

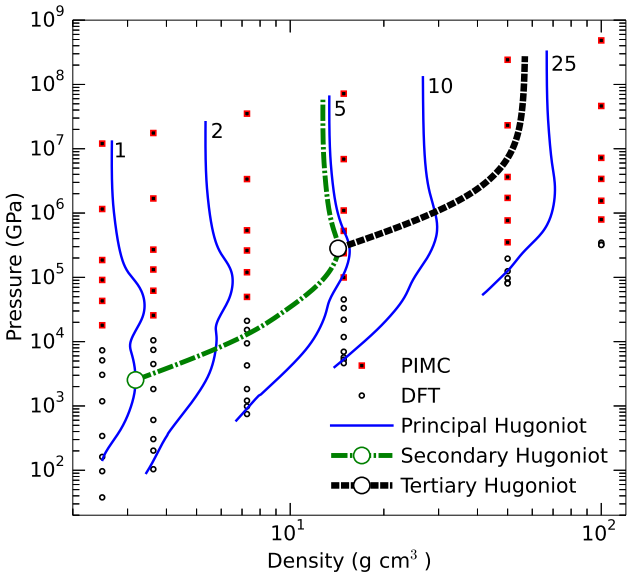

FIG. 12. Shock Hugoniot curves for different initial densities. The label on the curve specifies the ratio of the initial density to that of solid oxygen at 0K, 0.6671 g cm^{-3}. Secondary and tertiary Hugoniot curves are also plotted.

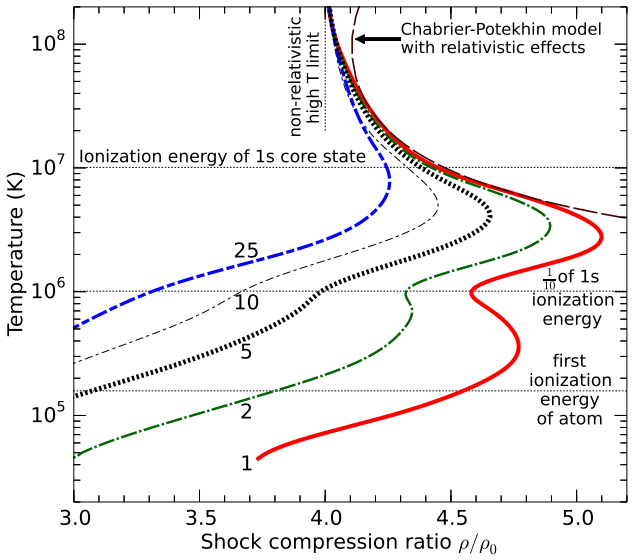

FIG. 13. Hugoniot curves for different pre-compression density ratios.

The resulting Hugoniot curve has been plotted in T-P and P-ρ spaces in Figs. 1 and 12, respectively.

Samples in shock wave experiments may be pre-compressed inside of a diamond anvil cell in order to reach much higher final densities than possible with a sample at ambient conditions. This technique allows shock wave experiments to probe density-temperature consistent with planetary and stellar interiors[74]. Therefore, we repeat our Hugoniot calculation starting with initial densities ranging from a 1 to a 25-fold increase of the ambient density. Figure 12 shows the resulting family of Hugoniot curves. While starting from the ambient density leads to a maximum shock density of 3.5 g cm^{-3}, a 25-fold pre-compression yields a much higher maximum shock density of 71 g cm^{-3}, as expected. However, such extreme densities can be reached more easily with triple shock experiments as our example in Fig. 12 illustrates. We used the first compression maximum on the principal Hugoniot curve (ρ =3.182 g cm^{-3}, P =2535 GPa, T = 358,600 K) as the initial state of the secondary Hugoniot curve. The compression maximum on this curve (ρ =14.25 g cm^{-3}, P =282000 GPa, T = 4,819,000 K) served as initial state for the tertiary Hugoniot curve.

Figure 13 shows the temperature dependence of the precompression density ratio for the five representative Hugoniot curves in Figure 12. In the high-temperature limit, all curves converge to a compression ratio of 4, which is the value of a nonrelativistic ideal gas. We

also include of the Hugoniot curve computed with the relativistic, fully-ionized Chabrier-Potekhin model, which shows the relativistic correction in the high-temperature limit. In general, the shock compression is determined by the excitation of internal degrees of freedom, which increases the compression, and interaction effects, which decrease the compression[75]. Consistent with our results for hydrogen, helium[47], and neon[50] we find that an increase in the initial density leads to a slight reduction in the shock compression (Figure 13) because particles interact more strongly at higher density.

The shock-compression ratio also exhibits two maxima as a function of temperature, which can be attributed to the ionization of electrons in the first and second shell. On the principal Hugoniot curve, the first maximum of ρ/ρ_0=4.77 occurs at temperature of 3.59×10^5 K (30.94 eV), which is above the first ionization energy of the oxygen atom, 13.61 eV, but less than the second ionization energy, 35.12 eV. A second compression maximum of ρ/ρ_0=5.10 is found for a temperature of 2.87×10^6 K (247.32 eV), which can be attributed to the ionization of the 1s core states of the oxygen ions. The 1s ionization energy is 871.41 eV. This is consistent with the ionization process we observe in Figure 7, where charge density around the nuclei is reduced over the range of $2 - 8 \times 10^6$ K. Since DFT-MD simulations, which use pseudopotentials to replace core electrons, cannot access physics about core ionization, PIMC is a necessary tool to determine the maximum compression along the principle Hugoniot curve.

VII. CONCLUSIONS

In this work, we have combined PIMC with DFT-MD to construct a coherent EOS for oxygen over wide range of densities and temperatures that includes warm dense matter and plasmas in stars and stellar remnants. The two methods validate each other in temperature range of 2.5×10^5–1×10^6 K, where both yield consistent results. We compared our equation of state at high temperature with the analytic models of Chabrier-Potekhin and Debye-Hückel. The deviations that we identified underline the importance for new methods like PIMC to be developed for the study of warm dense matter. Nuclear and electronic pair-correlations reveal a temperature- and pressure-driven ionization process, where temperature-ionization of the 1s state is suppressed while other states are efficiently ionized as density increases up to 100 $\mathrm{g\,cm^{-3}}$. Changes in the density of states confirms the temperature- and pressure-

ionization behavior observed in the pair-correlation data. Lastly, we find the ionization imprints a signature on the shock Hugoniot curves and that PIMC simulations are necessary to determine the state of the highest shock compression. Our and Hugoniot and equation of state will help to build more accurate models for stars and stellar remnants.

ACKNOWLEDGMENTS

We are grateful to Alexander Potekhin for helpful discussions about the fully ionized EOS. We are also grateful to Cyril Georgy for sharing his data and knowledge of massive star evolution. We are also grateful to Jan Vorberger for discussions on continuum lowering. This research is supported by the U. S. Department of Energy, grant de-sc0010517. Computational support was provided by NERSC, NASA, and the Janus supercomputer, which is supported by the National Science Foundation (Grant No. CNS-0821794), the University of Colorado, and the National Center for Atmospheric Research.

REFERENCES

[1]Y. A. Freiman and H. J. Jodl, Phys. Rep. **401**, 1 (2004).

[2]M. Santoro, E. Gregoryanz, H. k. Mao, and R. J. Hemley, Phys. Rev. Lett. **93**, 265701 (2004).

[3]L. F. Lundegaard and G. Weck and M. I. McMahon and S. Desgreniers and P. Loubeyre, Nature **443**, 201 (2006).

[4]A. F. Goncharov, N. Subramanian, T. R. Ravindran, M. Somayazulu, V. B. Prakapenka, and R. J. Hemley, J. Chem. Phys. **135**, 084512 (2011).

[5]Y. Ma, A. R. Oganov, and C. W. Glass, Phys. Rev. B **76**, 064101 (2007).

[6]J. Sun, M. Martinez-Canales, D. D. Klug, C. J. Pickard, and R. J. Needs, Phys. Rev. Lett. **108**, 045503 (2012).

[7]S. Desgreniers, Y. K. vohra, and A. L. Ruoff, J. Phys. Chem. **94**, 1117 (1990).

[8]Y. Akahama and H. Kawamura and D. Häusermann and M. Hanfland and O. Shimomura, Phys. Rev. Lett. **74**, 4690 (1995).

[9]S. Serra, G. Chiarotti, S. Scandolo, and E. Tosatti, Phys. Rev. Lett. **80**, 5160 (1998).

[10]B. Militzer and R. J. Hemley, Nature **443**, 150 (2006).

[11]K. Shimizu, K. Suhara, M. Ikumo, M. I. Eremets, and K. Amaya, Nature **393**, 767 (1998).

[12]J. B. Neaton and N. W. Ashcroft, Phys. Rev. Lett. **88**, 205503 (2002).

[13]S. Klotz, T. Strassle, A. L. Cornelius, J. Philippe, and T. Hansen, Phys. Rev. Lett. **104**, 115501 (2010).

[14]J. N. Bahcall and M. H. Pinsonneault, Phys. Rev. Lett. **92**, 121301 (2004).

[15]Private communication: courtesy of Cyril Georgy, University of Keele (United Kingdom).

[16]G. Fontaine and H. M. V. Horn, Astrophys. J. Suppl. S. **31**, 467 (1976).

[17]G. Fontaine, H. C. J. Graboske, and H. M. V. Horn, Astrophys. J. Suppl. S. **35**, 293 (1977).

[18]B. Hansen, Phys. Rep. **399**, 1 (2004).

[19]A. Burrows, W. B. Hubbard, J. I. Lunine, and J. Liebert, Rev. Mod. Phys. **73**, 719 (2001).

[20]W. B. Hubbard, A. Burrows, and J. I. Lunine, Annu. Rev. Astron. Astr. **40**, 103 (2002).

[21]T. Guillot, Annu. Rev. Earth Pl. Sc. **33**, 493 (2005).

[22]H. F. Wilson and B. Militzer, Astrophys. J. **745**, 54 (2012).

[23]S. Zhang, H. F. Wilson, K. P. Driver, and B. Militzer, Phys. Rev. B **87**, 024112 (2013).

[24]C. Hansen and S. Kawaler, *Stellar Interiors: Physical Principles, Structure, and Evolution*, Astronomy and astrophysics library, Vol. 1 (Springer-Verlag New York, 1994).

[25]J. J. Fortney, The Astrophys. J. Lett. **747**, L27 (2012).

[26]K. Lodders and J. B. Fegley, Icarus **155**, 393 (2002).

[27]M. Zoccali, A. Lecureur, B. Barbuy, V. Hill, A. Renzini, D. Minniti, Y. Momany, A. Gmez, and S. Ortolani, Astron. Astrophys. **457**, L1 (2006).

[28]M. H. Wong, J. I. Lunine, S. K. Atreya, T. Johnson, P. R. Mahaffy, T. C. Owen, and T. Ecnrenaz, Rev. Mineral. Geochem. **68**, 219 (2008).

[29]C. Needham, *Blast Waves*, Shock Wave and High Pressure Phenomena (Springer Berlin Heidelberg, 2010).

[30]G. Wallerstein, I. Iben, P. Parker, A. Boesgaard, G. Hale, A. Champagne, C. Barnes, F. Käppeler, V. Smith, R. Hoffman, F. Timmes, C. Sneden, R. Boyd, B. Meyer, and D. Lambert, Rev. Mod. Phys. **69**, 995 (1997).

[31]E. M. Burbidge, G. R. Burbidge, W. a. Fowler, and F. Hoyle, Rev. Mod. Phys. **29**, 547 (1957).

[32]M. Schmidt, Astrophys. J. **129**, 243 (1959).

[33]G. Fontaine, P. Brassard, and P. Bergeron, Publ. Astonomical Soc. Pacific **113**, 409 (2001).

[34]G. Chabrier, P. Brassard, G. Fontaine, and D. Saumon, Astrophys. J. **543**, 216 (2000).

[35]K. Lodders, Astrophys. J. **591**, 1220 (2003).

[36]N. Itoh, K. Kojo, and M. Nakagawa, Astrophys. J. Suppl. S. **74**, 291 (1990).

[37]M. Bastea, A. C. Mitchell, and W. J. Nellis, Phys. Rev. Lett. **86**, 3108 (2001).

[38]B. Militzer, F. Gygi, and G. Galli, Phys. Rev. Lett. **91**, 265503 (2003).

[39]W. J. Nellis and A. C. Mitchell, J. Chem. Phys. **73**, 6137 (1980).

[40]D. C. Hamilton, W. J. Nellis, A. Mitchell, F. H. Ree, and M. van Thiel, J. Chem. Phys. **88**, 5042 (1988).

[41]E. D. Chisolm, S. D. Crockett, and M. S. Shaw, AIP Conf. Proc. **1195**, 556 (2009).

[42]M. Ross and F. H. Ree, J. Chem. Phys. **73**, 6146 (1980).

[43]G. I. Kerley and A. C. Awitendick, *Shock Waves in Condensed Matter*, edited by Y. M. Gupta (Plenum, New York, 1986).

[44]Q. F. Chen, L. C. Cai, Y. Zhang, and Y. J. Gu, J. Chem. Phys. **128**, 104512 (2008).

[45]C. Wang and P. Zhang, J. Chem. Phys. **132**, 154307 (2010).

[46]G. Massacrier, A. Y. Potekhin, and G. Chabrier, Phys. Rev. E - Stat. Nonlinear, Soft Matter Phys. **84**, 1 (2011).

[47]B. Militzer, Phys. Rev. B **79**, 155105 (2009).

[48]K. P. Driver and B. Militzer, Phys. Rev. Lett. **108**, 115502 (2012).

[49]L. X. Benedict, K. P. Driver, S. Hamel, B. Militzer, T. Qi, A. A. Correa, and E. Schwegler, Phys. Rev. B **89**, 224109 (2014).

[50]K. P. Driver and B. Militzer, Phys. Rev. B **91**, 045103 (2015).

[51]D. M. Ceperley, Rev. Mod. Phys. **67**, 279 (1995).

[52]M. Koenig *et al.*, Plasma Phys. Contr. F. **47** (2005).

[53]E. L. Pollock, Comput. Phys. Commun. **52**, 49 (1988).

[54]D. M. Ceperley, J. Stat. Phys. **63**, 1237 (1991).

[55]B. Militzer and D. M. Ceperley, Phys. Rev. E **63**, 066404 (2001).

[56]See supplemental material at http://scitation.aip.org/? for time-step and finite-size convergence tables.

[57]D. Marx and J. Hutter, Modern methods and algorithms of quantum chemistry **1**, 301 (2000).

[58]E. W. Brown, B. K. Clark, J. L. DuBois, and D. M. Ceperley, Phys. Rev. Lett. **110**, 146405 (2013).

[59]D. N. Mermin, Phys. Rev. **137**, A1441 (1965).

[60]F. Lambert and J. Clérouin and S. Mazevet, Europhys. Lett. **75**, 681 (2006).

[61]G. Kresse and J. Furthmüller, Phys. Rev. B **54**, 11169 (1996).

[62]P. E. Blöchl, Phys. Rev. B **50**, 17953 (1994).

[63]J. P. Perdew, K. Burke, and M. Ernzerhof, Phys. Rev. Lett. **77**, 3865 (1996).

[64]X. Gonze, B. Amadon, P. M. Anglade, J. M. Beuken, F. Bottin, P. Boulanger, F. Bruneval, D. Caliste, R. Caracas, M. Côté, T. Deutsch, L. Genovese, P. Ghosez, M. Giantomassi, S. Goedecker, D. R. Hamann, P. Hermet, F. Jollet, G. Jomard, S. Leroux, M. Mancini, S. Mazevet, M. J. T. Oliveira, G. Onida, Y. Pouillon, T. Rangel, G. M. Rignanese, D. Sangalli, R. Shaltaf, M. Torrent, M. J. Verstraete, G. Zerah, and J. W. Zwanziger, Comput. Phys. Commun. **180**, 2582 (2009).

[65]N. A. W. Holzwarth, A. R. Tackett, and G. E. Matthews, Comput. Phys. Commun. **135**, 329 (2001).

[66]`http://elk.sourceforge.net/`.

[67]G. Chabrier and A. Y. Potekhin, Phys. Rev. E **58**, 4941 (1998).

[68]P. Debye and E. Huckel, Phys. Z. **24**, 185 (1923).

[69]`http://opium.sourceforge.net`.

[70]B. Militzer, J. Phys. A: Math. Theor. **42**, 214001 (2009).

[71]M. Cardona and L. Ley, eds., *Photoemission in Solids I: General Principles* (Springer-Verlag, Berlin, 1978).

[72]S. Root, R. J. Magyar, J. H. Carpenter, D. L. Hanson, and T. R. Mattsson, Phys. Rev. Lett. **105**, 085501 (2010).

[73]Y. B. Zeldovich and Y. P. Raizer, *Elements of Gasdynamics and the Classical Theory of Shock Waves* (Academic Press, New York, 1968).

[74]B. Militzer and W. B. Hubbard, AIP Conf. Proc. **955**, 1395 (2007).

[75]B. Militzer, Phys. Rev. Lett. **97**, 175501 (2006).

TABLE I. EOS table of oxygen pressures and internal energies at density-temperature conditions simulated in this work. The numbers in parentheses indicate the statistical uncertainties of the DFT-MD and PIMC simulations.

ρ ($\mathrm{g\,cm^{-3}}$)	T (K)	P (GPa)	E (Ha/atom)
2.48634[a]	1034730000	12031695(879)	44227(3)
2.48634[a]	99497670	1155684(608)	4242(2)
2.48634[a]	16167700	185881(73)	674.57(29)
2.48634[a]	8083850	91166(21)	323.90(9)
2.48634[a]	4041920	43037(12)	138.71(6)
2.48634[a]	2020960	17999(15)	16.06(7)
2.48634[a]	998004	7336(9)	−41.43(4)
2.48634[b]	1000000	7339(6)	−42.41(2)
2.48634[a]	748503	5118(11)	−50.66(4)
2.48634[b]	750000	5119(5)	−51.84(18)
2.48634[a]	500000	3044(11)	−59.30(4)
2.48634[b]	500000	3049(5)	−60.58(3)
2.48634[a]	250000	1189(12)	−66.94(5)
2.48634[b]	250000	1183(3)	−69.293(3)
2.48634[b]	100000	341(1)	−73.635(1)
2.48634[b]	50000	161(1)	−74.571(1)
2.48634[b]	30000	97(1)	−74.811(1)
2.48634[b]	10000	38(1)	−75.015(1)

TABLE I. (*Continued.*)

ρ (g cm^{-3})	T (K)	P (GPa)	E (Ha/atom)
3.63046[a]	1034730000	17566926(1904)	44223(5)
3.63046[a]	99497670	1685108(750)	4235(2)
3.63046[a]	16167700	269993(107)	669.34(28)
3.63046[a]	8083850	132427(35)	320.24(11)
3.63046[a]	4041920	61955(18)	132.56(6)
3.63046[a]	2020960	25689(28)	10.67(8)
3.63046[a]	998004	10569(14)	−42.93(4)
3.63046[b]	1000000	10507(14)	−44.13(2)
3.63046[a]	748503	7433(14)	−51.81(4)
3.63046[b]	750000	7443(8)	−52.79(5)
3.63046[a]	500000	4414(15)	−60.15(4)
3.63046[b]	500000	4483(5)	−61.412(6)
3.63046[b]	250000	1831(3)	−69.658(2)
3.63046[b]	100000	605(2)	−73.686(2)
3.63046[b]	50000	305(1)1	−74.565(1)
3.63046[b]	30000	202(2)	−74.797(1)
3.63046[b]	10000	104(1)	−74.992(1)

TABLE I. (*Continued.*)

ρ (g cm^{-3})	T (K)	P (GPa)	E (Ha/atom)
7.26176[a]	1034730000	35142831(2985)	44227(4)
7.26176[a]	99497670	3374099(1777)	4237(2)
7.26176[a]	16167700	538734(172)	664.43(26)
7.26176[a]	8083850	261808(75)	311.36(11)
7.26176[a]	4041920	120041(34)	119.03(5)
7.26176[a]	2020960	49637(51)	1.74(7)
7.26176[a]	998004	20964(31)	−45.53(4)
7.26176[b]	1000000	21301(20)	−46.16(4)
7.26176[a]	748503	15122(42)	−53.17(5)
7.26176[b]	750000	15236(21)	−54.51(2)
7.26176[a]	500000	9262(24)	−61.27(3)
7.26176[b]	500000	9424(10)	−62.652(7)
7.26176[a]	250000	4405(44)	−67.78(5)
7.26176[b]	250000	4268(5)	−70.098(2)
7.26176[b]	100000	1831(3)	−73.613(2)
7.26176[b]	50000	1210(2)	−74.382(2)
7.26176[b]	30000	986(5)	−74.606(2)
7.26176[b]	10000	749(1)	−74.813(1)

TABLE I. (*Continued.*)

ρ ($\mathrm{g\,cm^{-3}}$)	T (K)	P (GPa)	E (Ha/atom)
14.8632[a]	1034730000	71917073(5787)	44217(4)
14.8632[a]	99497670	6899765(3226)	4230(2)
14.8632[a]	16167700	1096035(364)	655.35(24)
14.8632[a]	8083850	527445(141)	299.20(10)
14.8632[a]	4041920	237350(67)	103.41(5)
14.8632[a]	2020960	99599(98)	−5.97(6)
14.8632[a]	998004	44297(52)	−47.32(3)
14.8632[b]	1000000	45274(64)	−47.95(4)
14.8632[a]	748503	32595(59)	−54.80(3)
14.8632[b]	750000	33293(69)	−55.76(4)
14.8632[a]	500000	21447(56)	−61.86(3)
14.8632[b]	500000	21945(35)	−63.21(1)
14.8632[b]	250000	11803(11)	−69.884(4)
14.8632[b]	100000	6975(7)	−72.907(3)
14.8632[b]	50000	5705(6)	−73.590(2)
14.8632[b]	30000	5239(4)	−73.815(1)
14.8632[b]	10000	4626(8)	−74.057(1)

TABLE I. (*Continued.*)

ρ ($\mathrm{g\,cm^{-3}}$)	T (K)	P (GPa)	E (Ha/atom)
50.0000[a]	1034730000	241912168(8061)	44208(1)
50.0000[a]	99497670	23165568(7204)	4215(1)
50.0000[a]	16167700	3638714(751)	633.85(14)
50.0000[a]	8083850	1721016(318)	272.08(6)
50.0000[a]	4041920	768044(164)	78.29(3)
50.0000[a]	2020960	351315(214)	−13.11(4)
50.0000[a]	998004	185345(210)	−46.12(4)
50.0000[c]	1000000	187281(611)	−47.36(11)
50.0000[c]	500000	118441(752)	−60.27(11)
50.0000[c]	250000	91835(1078)	−65.16(15)
50.0000[c]	100000	77796(541)	−67.49(7)
50.0000[c]	50000	75320(609)	−67.90(8)

TABLE I. (*Continued.*)

ρ ($\mathrm{g\,cm^{-3}}$)	T (K)	P (GPa)	E (Ha/atom)
100.000[a]	1034730000	483702750(18188)	44193(2)
100.000[a]	99497670	46258880(13163)	4201(1)
100.000[a]	16167700	7213882(1458)	617.35(13)
100.000[a]	8083850	3396956(706)	254.73(7)
100.000[a]	4041920	1553594(378)	68.31(4)
100.000[a]	2020960	793543(497)	−10.07(5)
100.000[a]	998004	490625(1050)	−40.28(10)
100.000[c]	1000000	490505(1367)	−41.78(12)
100.000[c]	500000	369913(2987)	−52.88(24)
100.000[c]	250000	326893(1556)	−56.75(12)
100.000[c]	100000	302710(1091)	−58.79(8)
100.000[c]	50000	298808(1064)	−59.13(8)

[a]PIMC

[b]VASP-MD

[c]ABINIT-MD with a small-core, PAW pseudopotentials

First-Principles Equation of State and Electronic Properties of Warm Dense Oxygen

K. P. Driver,[1] F. Soubiran,[1] Shuai Zhang,[1] and B. Militzer[1,2]
[1)] *Department of Earth and Planetary Science, University of California, Berkeley, California 94720, USA*[a)]
[2)] *Department of Astronomy, University of California, Berkeley, California 94720, USA*

(Dated: 22 January 2016)

arXiv:1601.05782v1 [physics.plasm-ph] 21 Jan 2016

I. CONVERGENCE TESTS

In this section, we provide raw data from our PIMC and DFT-MD time-step and finite-size convergence calculations. Table SI shows the results of static path integral Monte Carlo (PIMC) calculations for a 8-atom as a function of time-step for a fixed density. For a time-step of 0.00390625 Ha^{-1}, which we used in our production calculations, the results are well converged. The pressure has 0.3% error and internal energy has 0.3% error relative to the smallest time-step.

Table SII shows the comparison of pressures and internal energies for a 24-atom and 8-atom simulation cell as a function of temperature at a fixed density. Results are shown for both PIMC and density functional theory molecular dynamics (DFT-MD). The absolute difference between the 8-atom and 24-atom pressures and internal energies is only a fraction of a per cent of the total values, and often within the statistical error. As expected in DFT, the agreement between 8- and 24-atom results generally improves with temperature. Above 1×10^5 K, the 8-atom cell size is sufficient as the gamma-only k-point approximation becomes irrelevant.

[a)] Electronic mail: kdriver@berkeley.edu; http://militzer.berkeley.edu/~driver/

TABLE SI. Convergence of oxygen energy and pressure with respect to PIMC time-step for static calculation of an 8-atom cell at a fixed density and temperature.

ρ ($\mathrm{g\,cm^{-3}}$)	T(K)	Time-step ($\mathrm{Ha^{-1}}$)	P (GPa)	E (Ha/atom)
7.26176	1010479	0.015625	16700(45)	-51.30(4)
7.26176	1010479	0.0078125	17030(20)	-50.60(2)
7.26176	1010479	0.00390625	17200(30)	-50.17(3)
7.26176	1010479	0.00195312	17260(45)	-50.00(6)

TABLE SII. Comparison of oxygen pressures and internal energies computed for 24- and 8-atom simulations cells as a function of temperature at a fixed density and their relative absolute (ABS) errors. The numbers in parentheses indicate the one-sigma statistical uncertainties of the DFT-MD and PIMC simulations.

ρ ($\mathrm{g\,cm^{-3}}$)	T (K)	P (GPa) 24-atom cell	P (GPa) 8-atom cell	Δ P (GPa) ABS error	E (Ha/atom) 24-atom cell	E(Ha/atom) 8-atom cell	Δ E (Ha/atom) ABS error
7.26176[a]	1034730000	35139936(3207)	35142831(2985)	2895(4381)	44226(4)	44227(4)	1(6)
7.26176[a]	16167700	537967(253)	538734(172)	767(305)	664.3(3)	664.3(2)	0.0(4)
7.26176[a]	8083850	262087(87)	261808(75)	279(115)	312.2(1)	311.4(1)	0.79(3)
7.26176[a]	2020960	49881(56)	49637(51)	245(78)	2.3(1)	1.74(7)	0.52(1)
7.26176[a]	998004	21158(46)	20964(31)	195(55)	-44.95(5)	-45.53(4)	0.59(7)
7.26176[b]	1000000	21387(48)	21301(20)	85(52)	-46.11(6)	-46.16(4)	0.05(7)
7.26176[a]	750000	15033(54)	15122(42)	88(69)	-53.19(7)	-53.17(5)	0.03(8)
7.26176[b]	750000	15272(29)	15236(21)	37(36)	-54.49(3)	-54.51(2)	0.01(3)
7.26176[b]	500000	9433(14)	9424(10)	9(17)	-62.65(1)	-62.652(7)	0.00(1)
7.26176[b]	250000	4292(5)	4268(5)	24(7)	-70.089(3)	-70.098(2)	0.009(4)
7.26176[b]	100000	1831(3)	1765(6)	66(7)	-73.613(2)	-73.663(4)	0.050(4)
7.26176[b]	50000	1210(2)	1107(4)	103(4)	-74.382(1)	-74.448(2)	0.066(2)

[a] PIMC
[b] DFT-MD